Numer. Math. Theor. Meth. Appl.
doi: 10.4208/nmtma.2017.s01

Vol. **10**, No. 2, pp. 205-221
May 2017

Defects Around a Spherical Particle in Cholesteric Liquid Crystals

Yu Tong, Yiwei Wang and Pingwen Zhang*

Laboratory of Mathematics and Applied Mathematics, School of Mathematical Sciences, Peking University, Beijing 100871, China

Received 2 November 2016; Accepted (in revised version) 5 January 2017

Dedicated to Professor Zhenhuan Teng on the occasion of his 80th birthday

Abstract. We investigate the defect structures around a spherical colloidal particle in a cholesteric liquid crystal using spectral method, which is specially devised to cope with the inhomogeneity of the cholesteric at infinity. We pay particular attention to the cholesteric counterparts of nematic metastable configurations. When the spherical colloidal particle imposes strong homeotropic anchoring on its surface, besides the well-known twisted Saturn ring, we find another metastable defect configuration, which corresponds to the dipole in a nematic, without outside confinement. This configuration is energetically preferable to the twisted Saturn ring when the particle size is large compared to the nematic coherence length and small compared to the cholesteric pitch. When the colloidal particle imposes strong planar anchoring, we find the cholesteric twist can result in a split of the defect core on the particle surface similar to that found in a nematic liquid crystal by lowering temperature or increasing particle size.

AMS subject classifications: 65N35, 76A15

Key words: Cholesteric liquid crystal, defects, Landau-de Gennes theory, spectral method.

1. Introduction

Dispersing colloidal particles in liquid crystals usually disrupts the orientation order and leads to formation of topological defects around each particle. These topological defects play a important role in the long-range interaction between particles, which determines the self-assembled structures of the colloids-liquid crystals composite materials [6, 24]. Therefore much attention has been paid to the defect configurations around colloidal particles.

*Corresponding author. *Email addresses:* tong_yu@pku.edu.cn (Y. Tong), yiweiwang@pku.edu.cn (Y. W. Wang), pzhang@pku.edu.cn (P. W. Zhang)

The defect configurations around one spherical particle in a nematic liquid crystal are extensively studied by both experiments and simulations [9,19,28,29]. For a spherical particle with strong homeotropic anchoring, two types of metastable configurations are found, known as dipole and Saturn ring. And for strong planar anchoring, three types of boojums will arise, known as single-, double- and split-cores [32]. For the cholesteric case, relatively little work has been done even for the one spherical particle case.

The theories that widely used to describe the liquid crystals can be classified into three levels [12]: the molecular theory, the Q-tensor theory and the vector theory. The vector theory, such as the Oseen-Frank theory [26] and the Ericksen's theory [5], uses unit-vectors $\mathbf{n}(\mathbf{x})$ as an order parameter, called "director", to describe the average orientation of molecules in the vicinity of each point $\mathbf{x}$. The vector theory gives a simple description of liquid crystals. However, it fails to preserve the head-to-tail symmetry of liquid crystals [1] and cannot be used to study the detailed structures of defects. The molecular theory [25], which uses an orientational distribution function $f(\mathbf{x},\mathbf{n})$ as an order parameter, gives the precise description of liquid crystals, but simulations based on it involve large computational cost. The the Q-tensor theory, such as the Landau-de Gennes theory [4], uses a 3×3 symmetric traceless tensor $\mathsf{Q}(\mathbf{x})$ as an order parameter. The Q-tensor theory enjoys the benefit that Q is continuous around defects and it gives a physically realistic description of liquid crystals.

There are some simulation studies devoted to investigate the defect structures around a spherical particle in a cholesteric liquid crystal within Landau-de Gennes theory. By using lattice Boltzmann method (LBM), a twisted Saturn ring configuration is reported with strong homeotropic anchoring on the particle surface [16]. A pair of defect patches or helical disclination lines that link the point defects on particle surface are reported for strong planar anchoring [17]. Besides, the Monte Carlo simulations have also been used to study these problems [22].

It is easy to understand the twisted Saturn ring found in a cholesteric, which can be regarded as the nematic Saturn ring undergoing a twist. Then a natural question is, what will dipole become in a cholesteric? Recently, a dipole-like profile around colloidal particle in a cholesteric liquid crystal has been reported in the confinement-unwound homeotropic cells, found through experiments and numerical simulations with finite difference method [27]. However, the structure they studies is in a bounded domain between two glass plates, and the perpendicular anchoring on glass plates here plays a dominant role, forcing a uniform director field far away from the particle, which is in contrast with the layer structure in the cholesteric.

Also, the helical disclination lines can be realized by moving the two point defects of a split-core away from each other and wrapping the disclination line around the particle. But will the nematic single- and double-cores lead to the same configuration after applying cholesteric twist?

The questions mentioned above motivate us to study these problems within the Landau-de Gennes theory using spectral method. One of the difficulties of solving these problems numerically is that the size of the defect core may be much smaller than the

https://doi.org/10.4208/nmtma.2017.s01

radius of colloidal particle [10]. It requires very fine grids to capture the detailed structure of defects. Though the adaptive mesh refinement (AMR) [9] can solve this difficulty partially, due to the high computational cost, it is difficult to apply it to the cholesteric case where there is no rotational symmetry to utilize. As the domain we study, which after non-dimensionalization is the space outside the unit sphere, is very simple, we can apply the spectral method, which is a high-accuracy global method that enables us to capture the fine structures of defects with relatively little computational costs. Besides, the spectral method also enables us to implement the simulation on the whole unbounded domain.

In our simulation, for strong homeotropic anchoring, we find a defect configuration corresponding to the nematic dipole around a particle in unbounded region. We explore the detailed structure of the defect and then its free energy as compared to the twisted Saturn ring for different values of non-dimensionalized parameters. For strong planar anchoring, we find a twist-driven split of the cores that transforms single-cores to double-cores and then split-cores, enabling the emergence of helical disclination lines by further increasing the twist.

The rest of the paper is organized as follows. In Section 2, we describe the Landau-de Gennes model we use. In Section 3, we present our numerical method, paying special attention to our way of dealing with the inhomogeneity at infinity. The numerical results are presented in Sections 4 and 5, in which we discuss the various defect configurations for strong homeotropic and planar anchoring.

2. Model description

In Landau-de Gennes theory, the orientational order of liquid crystal is described by a 3×3 symmetric traceless tensor $\mathsf{Q}(\mathbf{x})$ defined as

$$\mathsf{Q}(\mathbf{x}) = \int_{\mathbb{S}^2} \Big(\mathbf{n} \otimes \mathbf{n} - \frac{1}{3}\mathsf{I}\Big)\rho(\mathbf{x}, \mathbf{n})\mathrm{d}\mathbf{n}, \tag{2.1}$$

where $\rho(\mathbf{x}, \mathbf{n})$ is the probability density of orientation $\mathbf{n}$ at $\mathbf{x}$, satisfying

$$\rho(\mathbf{x}, \mathbf{n}) \geq 0, \quad \rho(\mathbf{x}, \mathbf{n}) = \rho(\mathbf{x}, -\mathbf{n}), \quad \int_{\mathbb{S}^2} \rho(\mathbf{x}, \mathbf{n})\mathrm{d}\mathbf{n} = 1. \tag{2.2}$$

The free energy of Landau-de Gennes theory in cholesteric liquid crystals can be written as

$$\mathcal{F}(\mathsf{Q}, \nabla\mathsf{Q}) = \int_{\Omega} \left(f_b(\mathsf{Q}) + f_e(\mathsf{Q}, \nabla\mathsf{Q})\right) \mathrm{d}\mathbf{x} + \mathcal{F}_s, \tag{2.3}$$

with f_b and f_e as the bulk and elastic energy densities, given by

$$f_b(\mathsf{Q}) = c\mathrm{tr}\mathsf{Q}^2 - \sqrt{6}b\mathrm{tr}\mathsf{Q}^3 + a(\mathrm{tr}\mathsf{Q}^2)^2, \tag{2.4a}$$

$$f_e(\mathsf{Q}, \nabla\mathsf{Q}) = \frac{K_0}{4}|\nabla \cdot \mathsf{Q}|^2 + \frac{K_1}{4}|\nabla \times \mathsf{Q} + 2q_0\mathsf{Q}|^2, \tag{2.4b}$$

https://doi.org/10.4208/nmtma.2017.s01

where a, b and c are material dependent parameters, K_0 and K_1 are elastic constants [8] and $|\cdot|$ is the Frobenius norm.

The surface term is added to impose boundary conditions on the surface of the colloidal particles. For strong homeotropic anchoring, the surface energy can be written as

$$\mathcal{F}_s = \frac{1}{2}w\int_{\partial\Omega}|\mathsf{Q}(\mathbf{x})-\mathsf{Q}_b(\mathbf{x})|^2\mathrm{d}S, \tag{2.5}$$

where $Q_b = S_0(\mathbf{n}_b\otimes\mathbf{n}_b - \frac{1}{3}\mathsf{I})$ and $\mathbf{n}_b$ is the given director field on the surface. $S_0 > 0$ is the uniaxial order parameter that minimizes the bulk energy [20]. For strong planar anchoring, the directors on the surface are free to rotate around the normal vector, but are kept to be tangential to the surface. The surface energy can be written as

$$\mathcal{F}_s = \frac{1}{2}w\int_{\partial\Omega}\left|\left(\mathsf{Q}+\frac{S_0}{3}\mathsf{I}\right)\mathbf{x}\right|^2\mathrm{d}S, \tag{2.6}$$

where $|\cdot|$ is the Euclidean norm of vectors. This boundary condition is the special case of the famous surface energy proposed by Fournier and Galatola [7] (with $W_2 = 0$ in Eq. (6) of that paper) [14]. The surface energy (2.6) can be understood in the following way: we constrain the normal vector on the surface to be a eigenvector corresponding to a negative eigenvalue λ_ν (we choose $\lambda_\nu = -\frac{1}{3}S_0$ as in [14]), and hence the director, which is the eigenvector corresponding to the largest eigenvalue, has to be tangential to the surface.

It is convenient to non-dimensionalize the free energy in the following discussion. We first take the radius of particle R as the unit length, and let $\tilde{\mathsf{Q}} = (b/a)\mathsf{Q}$. Removing the tilde and redundant coefficient, the reduced free energy density becomes

$$\begin{aligned} f(\mathsf{Q},\nabla\mathsf{Q}) =& \frac{1}{16}\tau\mathrm{tr}(\mathsf{Q}^2) - \frac{\sqrt{6}}{4}\mathrm{tr}(\mathsf{Q}^3) + \frac{1}{4}\mathrm{tr}(\mathsf{Q}^2)^2 \\ &+ \frac{\xi^2}{2R^2}(|\nabla\times\mathsf{Q}+\tilde{R}\mathsf{Q}|^2 + \eta|\nabla\cdot\mathsf{Q}|^2), \end{aligned} \tag{2.7}$$

where $\tilde{R} = 2q_0R = 4\pi R/p$ and $\eta = K_0/K_1$.

We focus on three main dimensionless parameters in our simulation: the dimensionless temperature $\tau = 4ac/b^2$ (nematic-isotropic transition at $\tau = 1$), R/ξ and R/p, where $\xi = (aK_1/8b^2)^{1/2}$ is the nematic coherence length, and $p = 2\pi/|q_0|$ is the cholesteric pitch. The definitions of τ and ξ are consistent with those in [9, 32]. Another dimensionless parameter we shall use is $\kappa = 8\xi^2q_0^2$, measuring chirality. In our simulation, we shall always set $\eta = 1$ and take $w \gg 1$, though our numerical method can also be used to study the effect of η and w.

Similar to the nematic case, we can use the following quantities to visualize the defect structures. First is the biaxial coefficient β. In Landau-de Gennes theory, in which the Q is continuous everywhere, defects are described as discontinuities of eigenvetor corresponding to the largest eigenvalue [4], which can only occur at the biaxial-uniaxial, uniaxial-isotropic or biaxial-isotropic interfaces (necessary condition) [15]. A

https://doi.org/10.4208/nmtma.2017.s01

simple way to find such interface is to use the biaxial coefficient in the physical literature β [23], which is defined by

$$\beta(\mathsf{Q}) = 1 - 6\frac{(\mathrm{tr}\mathsf{Q}^3)^2}{(\mathrm{tr}\mathsf{Q}^2)^3}. \tag{2.8}$$

It can be proved that $\beta \in [0,1]$, $\beta \neq 0$ for biaxial region and $\beta = 0$ for uniaxial region [21]. We can define $\beta = 0$ for the isotropic region, in which $\mathsf{Q} = 0$.

Besides, the defect loops can be visualized by the iso-surface of scalar order parameter S [30], and the iso-surface of Westin metrics c_l [3].

The scalar order parameter S is the largest eigenvalue of Q. As the scalar order parameter $S = 0$ at the defects and $S = S_0$ away from the defect cores, many previous physical studies use the iso-surfaces of $S = S_1$ with $0 < S_1 < S_0$ to visualize the defect loops [30], where S_1 should be chosen properly.

The definition of the Westin metrics can be found in [3]. We only use c_l, which is the difference between the two largest eigenvalues, in our visualization. Since $c_l = 0$ at defects, we can draw the iso-surfaces of $c_l = \delta$ for a small constant δ to indicate the positions of defects.

3. Numerical method

Our goal is to find the minimizer of the free energy (2.7). However, directly integrating the reduced free energy density over the unbounded region outside the particle (which is the unit sphere because of our choice of unit length) will yield no meaningful result. This can be solved by finding the ground state Q_0 and the corresponding free energy density for an undistorted cholesteric liquid crystal.

We assume the periodic direction of the cholesteric host is along the z-axis and we can denote the ground state as $\mathsf{Q}_0(z)$. Without loss of generality we can assume that $\mathsf{Q}_0(z)$ takes the following form [11, 13]:

$$\mathsf{Q}_0(z) = \sqrt{2}C_0\left(\mathbf{n}(z)\otimes\mathbf{n}(z) - \frac{1}{2}\mathsf{I}_2\right) + \sqrt{\frac{3}{2}}C_1\left(\mathbf{e}_3\otimes\mathbf{e}_3 - \frac{1}{3}\mathsf{I}_3\right), \tag{3.1}$$

where $\mathbf{n}(z) = (\cos(\tilde{R}z/2+\psi), \sin(\tilde{R}z/2+\psi), 0)$ is the ground state for Oseen-Frank theory [2], $\mathbf{e}_3 = (0,0,1)$, $\mathsf{I}_2 = \mathrm{diag}(1,1,0)$, $\mathsf{I}_3 = \mathrm{diag}(1,1,1)$. We shall always set $\psi = 0$, as the change of ψ is equivalent to rotating the coordinate system.

According to the previous studies [13, 18], the expression (3.1) is valid for low temperature and low chirality (which means that the dimensionless parameter κ is small). It can be verified that $\mathsf{Q}_0(z)$ we use here is a solution to the Euler-Lagrange equations obtained by minimizing the free energy in one period with periodic boundary condition. In our simulation, we only consider the values of temperature and chirality in the valid region of expression (3.1).

Substituting (3.1) into (2.7), we can obtain the values of C_0, C_1 and $f(\mathsf{Q}_0, \nabla\mathsf{Q}_0)$, which depends on the dimensionless temperature τ and the chirality κ, by numerically

https://doi.org/10.4208/nmtma.2017.s01

minimizing the function of two variables

$$f(\mathsf{Q}_0, \nabla\mathsf{Q}_0) = f(C_0, C_1) = \frac{1}{4}\Big[\frac{\tau}{4}(C_0^2 + C_1^2) + (3C_0^2C_1 - C_1^3) + (C_0^2 + C_1^2)^2 + \kappa C_1^2\Big]. \quad (3.2)$$

This is an algebraic function whose global minimizer can be easily calculated to high precision using Newton method.

It should be remarked that due to the symmetry of spherical particle, changing the periodic direction does not change the physical properties in the system we consider. Therefore, in our simulation, we can choose the periodic direction for consideration of efficiency of our numerical method, which we will explain in more detail later.

The assumption that the disturbance caused by the intrusion of colloidal particles decays at infinity ($\mathsf{Q} - \mathsf{Q}_0 \to 0$ as $r \to +\infty$), enables us to define a meaningful free energy and design the numerical method. The revised free energy measuring the elastic distortion caused by colloidal particles can be written as

$$\mathcal{F}[\mathsf{Q}] = \int_\Omega (f(\mathsf{Q}, \nabla\mathsf{Q}) - f(\mathsf{Q}_0, \nabla\mathsf{Q}_0))\,\mathrm{d}V. \quad (3.3)$$

If $\mathsf{Q} - \mathsf{Q}_0$ decays to 0 at infinity quickly enough, this functional will yield a finite result.

We use the spectral method to solve this problem. Since the physical domain $\Omega = \mathbb{R}^3\backslash B(0,1)$ we study is unbounded, we use exponential mapping to map it onto a bounded domain [31]. The mapping between the computational domain (ρ, θ, φ) and the physical domain (r, θ, φ) are given by

$$r = \sinh\left(\frac{\rho+1}{2}L\right) + 1, \quad \rho \in [-1, 1], \quad (3.4)$$

where r is the radial distance in the spherical coordinates.

The exponential mapping combines truncation (at $r = \sinh L + 1$) and mapping in dealing with the spectral approximation in unbounded domain [31]. We choose L so that $\sinh L + 1 = 10$ in most of our simulations. Our numerical tests show that no significant change of numerical results will occur by increasing L further.

It should be pointed out that the classical orthogonal systems on the unbounded domain, such as Laguerre polynomials, cannot be a proper choice for our problem due to the properties of $\mathsf{Q} - \mathsf{Q}_0$.

As $\mathsf{Q} - \mathsf{Q}_0$ decays to 0 when r grows to infinity for given Q_0, we ensure this by setting $\mathsf{Q} = \mathsf{Q}_0$ for $r \geq \sinh L + 1$ in our numerical procedure. This is realized by adding another boundary condition $\mathsf{Q} = \mathsf{Q}_0$ at $r = \sinh L + 1$.

Therefore the elements of $\mathsf{Q} - \mathsf{Q}_0$ can be regarded as functions on the computational domain $[-1, 1] \times \mathbb{S}^2$. We can expand each element of $\mathsf{Q} - \mathsf{Q}_0$ on the following basis

$$q^s = \sum_{n=0}^{\infty}\sum_{l=0}^{\infty}\sum_{m=-l}^{l} A_{nlm}^{(s)} L_n(\rho) Y_l^m(\theta, \phi), \quad (3.5)$$

https://doi.org/10.4208/nmtma.2017.s01

where $L_n(\rho)$ are the normalized Legendre polynomials, $Y_l^m(\theta,\phi)$ are the spherical harmonics, q^s are elements in $\mathsf{Q}-\mathsf{Q}_0$. Due to the traceless property and symmetry of Q-tensor, only five elements in $\mathsf{Q}-\mathsf{Q}_0$ need to be expanded.

Removing the higher-order terms in expression (3.5), the functional in expression (3.3) is a function of $A^{(s)}_{nlm}$, $0\le n\le N-1$, $0\le l\le L-1$, $-l\le m\le l$. Numerically optimizing this function using LBFGS with respect to $A^{(s)}_{nlm}$, we can obtain the metastable state as characterized by the value of Q-tensor in the entire region. The boundary conditions, both on the particle surface and at $r=\sinh L+1$, are expressed by penalty terms in the functional, whose coefficient is gradually increased to ensure that boundary conditions are satisfied. Integrations on ρ and $\cos\theta$ are done using Gauss-Legendre quadrature, and integrations on ϕ are done using composite trapezoid rule.

4. Numerical results

By setting $\tilde{R}=0$ in expression (2.7), we can obtain the metastable defect configurations around a spherical particle in a nematic liquid crystal, including the Saturn ring and dipole for strong homeotropic anchoring, and single-, double-, and split-core for strong planar anchoring. To find the cholesteric configuration corresponding to each nematic one, we use the disturbance of the Q-tensor of the nematic liquid crystal, which is $\mathsf{Q}-\mathsf{Q}_0$, as the initial value for the numerical optimization. In this way we can investigate the effect of the cholesteric twist on the nematic defect configurations.

4.1. Strong homeotropic anchoring

Applying the strong homeotropic anchoring condition on the colloidal particle surface, two types of defect configurations can be obtained in a cholesteric liquid crystal: twisted Saturn ring (Figs. 1(a)-(c)) and cholesteric dipole (Figs. 1(d)-(f)).

As mentioned before, the choice of the periodic direction affects the number of terms needed in the expansion of q^s in (3.5) to have sufficient numerical precision, thereby affecting the efficiency of our method. For cholesteric dipole, we choose x-direction as the periodic direction. The dipoles in Figs. 1 and 3 are obtained in this way. For twisted Saturn ring, we choose z-direction as the periodic direction when R/p is large and choose x-direction as the periodic direction for small R/p. As a general rule, the periodic direction is chosen by comparing the free energies calculated with the same basis and selecting the one with lower energy. However, for the sake of consistency and clarity, we will always use z-direction as the periodic direction when discussing the numerical results.

The twisted Saturn ring is already found by simulation in [16]. We successfully reproduced this type of defect structure as validation of our algorithm. This configuration can be regarded as the nematic Saturn ring after undergoing a twist along the periodic direction of the cholesteric host. On the xy-plane the orientation profile is similar to that on the xy-plane in a nematic host, as can be seen in Fig. 1(c). Fig. 2 shows the

https://doi.org/10.4208/nmtma.2017.s01

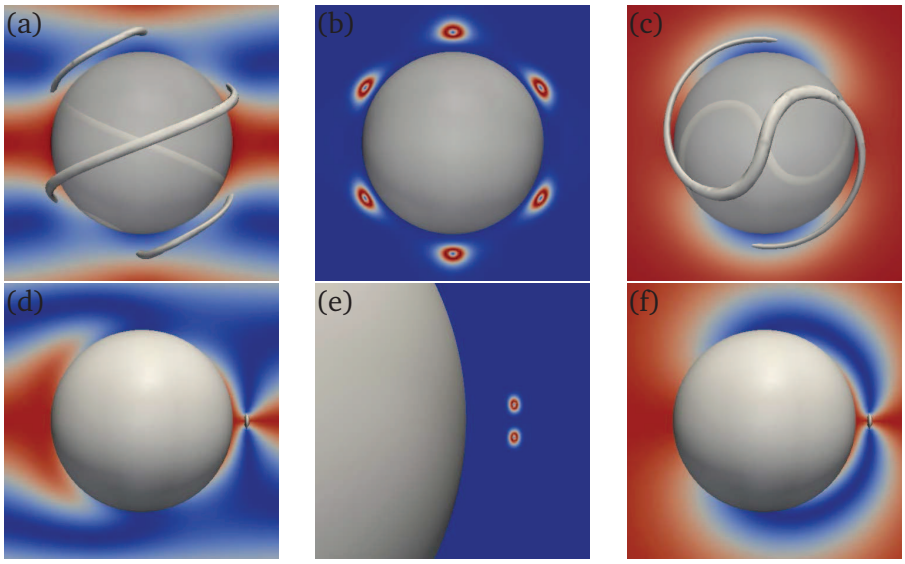

Figure 1: Two possible configurations around a spherical particle: (a)-(c) The defect structures in the twisted Saturn ring ($\tau = 0$, $R/\xi = 11.62$). (d)-(f) The defect structures in the cholesteric dipole ($\tau = -20.79$, $R/\xi = 59.34$). (a) and (d) Side-views with background color representing Q_{xx}. (b) and (e) Side-views with background color representing β. Red region has high biaxiality. (c) and (f) Top views with background color representing Q_{xx}. Defect lines are visualized by the iso-surfaces of c_l.

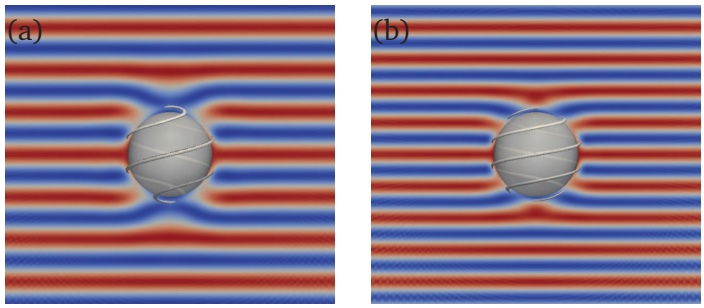

Figure 2: Twisted Saturn ring around colloidal particle. (a) $R/p = 1/2$, (b) $R/p = 2/3$. The background color represents the value of Q_{xx}, characterizing the layer structure of cholesteric host. Defect lines are visualized by iso-surfaces of c_l.

twisted Saturn rings for different values of R/p, which agree with the numerical results in [16].

From Fig. 2, we can see that the layer structure of the cholesteric host is only disturbed in the immediate vicinity of the particle, and disturbance becomes almost invisible when the distance to the particle is as small as $2R$, which confirms our assumption that $\mathsf{Q} - \mathsf{Q}_0$ vanishes rapidly when r increases.

By our method, we can capture the biaxiality in the vicinity of disclination lines. Fig. 1(b) shows that the disclination lines are wrapped by a region of high biaxiality, but

https://doi.org/10.4208/nmtma.2017.s01

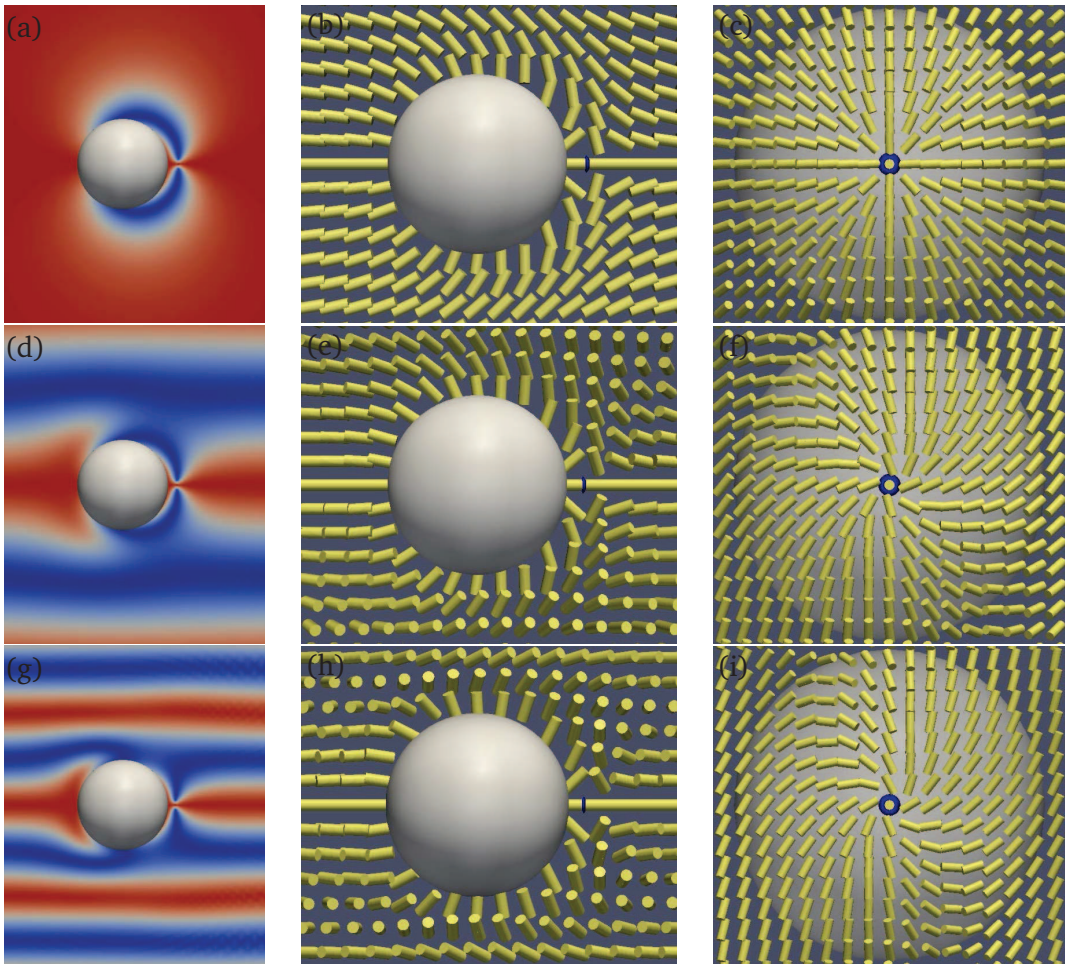

Figure 3: (a), (d) and (g) Orientation profiles on the xz-plane, with color representing Q_{xx}. (b), (e) and (h) Director fields on the xz-plane. (c), (f) and (i) Directors on the plane on which the defect loop is located. The defect loops are represented by iso-surfaces of c_l colored blue. $R/p = 0, 1/8, 1/4$ from top to bottom.

on the disclination lines the biaxiality is low. The Q-tensor on points further away from the disclination lines are almost uniaxial, although there is still spontaneous biaxiality as a result of cholesteric twist.

Besides the twisted Saturn ring configuration, we find another configuration, which corresponds to the nematic dipole. This defect configuration consists of a $-1/2$ defect loop on one side of the sphere like in the nematic case, as shown in Figs. 1(d)-(f). We shall hereafter refer to this defect configuration as cholesteric dipole, because of its similarity with the nematic dipole.

Fig. 3 shows the numerical result obtained for the cholesteric dipole for different R/p. The other dimensionless parameters for the figures are as follow: $\tau = -20.79$, $R/\xi = 59.34$. The dimensionless temperature is set relatively low to ensure the stability

https://doi.org/10.4208/nmtma.2017.s01

of nematic hedgehog under a wide range of R/ξ. Different values of R/p are tested as stated in the figures.

On the xy-plane, the director field of the far-field Q_0 is homogeneous. Therefore we can talk about a far-field orientation on the plane. Hence the orientation profile on the plane (Fig. 1(f)) is almost identical with the profile of nematic dipole (Fig. 3(a)). When the ratio R/p is small, the orientation profile in the vicinity of the colloidal particle closely resembles that in the nematics, as the directors of the far-field solution Q_0 are almost in the same direction near the particle. This can be seen by plotting the value of Q_{xx}, as shown in Fig. 3(d).

When the ratio R/p increases, the layer structure of the cholesteric host becomes increasingly predominant. For $R/p = 1/4$, which means the spatial period is equal to the diameter of the particle, we find the two "arms" that can be seen in profiles of nematic and cholesteric dipoles extending from the colloidal particle to the defect loop (e.g., the blue regions extending from the particles in Figs. 3(a) and (d)) are almost completely overshadowed by the layer structure. And the dipolar configuration loses its stability when R/p is large enough.

By looking at the director field around the colloidal particle (as shown in Fig. 3), we can also observe the coupling of the profile of nematic dipole with cholesteric layer structure. On the xz-plane (Figs. 3(e) and (h), compared with the nematic case in Fig. 3(b)), we can see that the directors tend to rotate along z-direction, and they are no longer confined on the plane as in nematics. The director field on xz-plane also distinguishes the cholesteric dipole found in our simulation from that in [27], in which a double-twist tube interspaces the particle and defect loop, while in our case no such tube is found. This may be attributed to the fact that the simulation and experiments of [27] are conducted in confinement-unwound cells with normal surface anchoring. Therefore our result is essentially different from the dipolar defect loop configuration found in [27].

On the plane containing the defect loop, the directors form a vortex structure in the vicinity of the loop as a result of cholesteric twist (Figs. 3(f) and (i)), as compared with the nematic case where all directors point outward (or inward, equivalently) (Fig. 3(c)). But the vortex structure does not form a skyrmion as in [27]. It can be seen that the rotation of the vortex intensifies with the increase of R/p. Again, rotation along the periodic direction is visible on the plane.

In our simulation, we find that the twisted Saturn ring configuration and cholesteric dipole coexist for certain range of values of dimensionless parameters. Therefore a comparison of free energy between the two configurations is needed. We are primarily interested in the effect of the two ratios R/ξ and R/p on the energetic preferability of the two configurations. Fig. 4 shows the value of $(F_{SR} - F_D) \times R^2/\xi^2$, where F_{SR} denotes the rescaled reduced free energy of twisted Saturn ring, and F_D that of cholesteric dipole. The energy difference is multiplied by R^2/ξ^2 so that the coefficient of the elastic term in the reduced free energy density is always equal to $1/2$. For each curve (with fixed R/p), we can see that $(F_{SR} - F_D) \times R^2/\xi^2$ increases with the increase of R/ξ, and this agrees with the result for nematic liquid crystals [9]. The curves move downward

https://doi.org/10.4208/nmtma.2017.s01

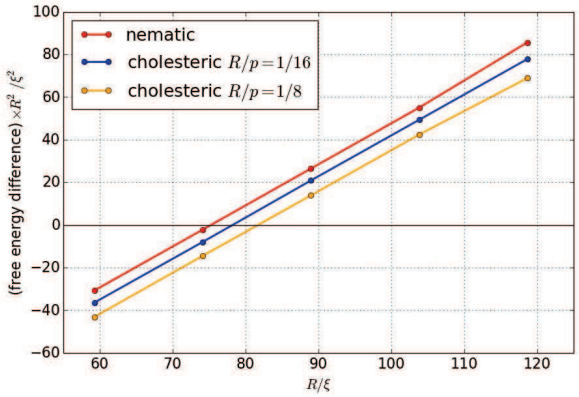

Figure 4: Free energy difference between the twisted Saturn ring and cholesteric dipole for different R/xi. The curves show the values of $(F_{SR} - F_D) \times R^2/\xi^2$.

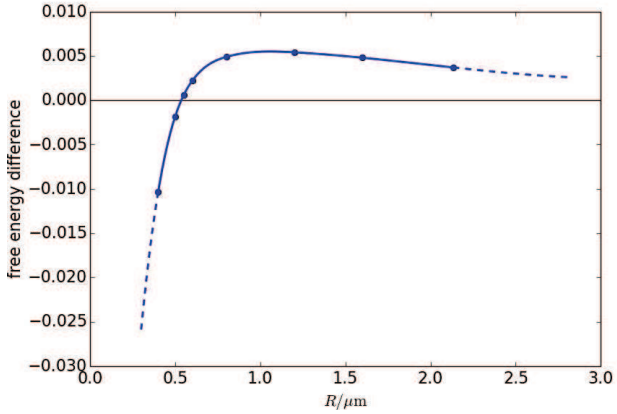

Figure 5: Free energy difference between the twisted Saturn ring configuration and dipolar defect loop configuration for different R/p. The curves show the values of $F_{SR} - F_D$.

when R/p is increased, as can be seen by comparing the three curves. Therefore we can conclude that the cholesteric dipole is favored when R/ξ is large and R/p small.

It may be easier in terms of experiment to change only one physical parameter. By increasing R and fixing all other physical parameters, we have Fig. 5, showing the free energy difference between the two types of configurations. The other physical parameters are fixed at $p = 6.4\mu\text{m}$ and $\xi = 6.74\text{nm}$.

In Fig. 5, it can be noticed that the free energy of the cholesteric dipole is lower than that of the twisted Saturn ring when $R > 5.4\mu\text{m}$. The initial gradual increase of $F_{SR} - F_D$ is a result of the increase of R/ξ, as described in Fig. 4. R/p is small initially and therefore does not play a significant role. $F_{SR} - F_D$ decreases when R is increased. This may be due to firstly the decreasing coefficient of elastic energy, and secondly the effect of increasing R/p, which tends to make twisted Saturn ring more

https://doi.org/10.4208/nmtma.2017.s01

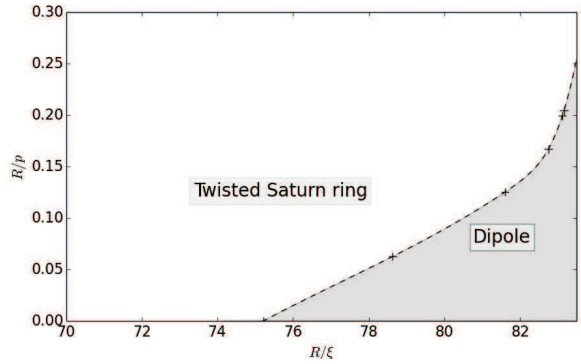

Figure 6: Phase diagram for the parameters R/ξ and R/p. The region in which dipolar defect loop is preferable to twisted Saturn ring in terms of energy is colored grey.

favorable. However, what will happen if we increase R further is still not clear, as the greater the values R/p and R/ξ are, the larger the required number of terms in the expansion of $\mathrm{Q} - \mathrm{Q}_0$ will be, hence it is computationally expensive to explore such situations. Although we have evidence showing that fixing R/ξ, when R/p is large (e.g., $R/p = 2/3$), the cholesteric dipole becomes no longer stable, it is not clear when simultaneously increasing R/ξ and R/p which one will outweigh the other.

The phase diagram shown in Fig. 6 gives us more insight into the roles played by the parameters. It can be seen that the region in which the cholesteric dipole is favored is located in the lower-right corner of the phase diagram, which agrees with our previous observation that the cholesteric dipole is preferred when R is large as compared to p and small as compared to ξ. However, we only consider a relatively small range of value for the parameters, as computational cost to determine the phase boundary is still high. We will address this problem in future work and give a more accurate phase boundary for a larger region of parameters.

4.2. Strong planar anchoring

Applying the strong planar anchoring on the colloidal particle surface, we obtain the handle-like helical disclination lines for large R/p, which are shown in Fig. 7 for $R/p = 1/2$ and $R/p = 1$.

The handle-like helical disclination lines have been reported in [17]. By Poincare's theorem, it is impossible to obtain a continuous director field on the surface of the colloidal particle. Therefore defects will occur on the particle surface, and in most cases extend into the host liquid crystals. The handle-like helical disclination lines arise naturally from the split-core configuration in nematics by moving the $+1/2$ defects away from each other on the surface, and linking them with the disclination lines. When the defects are sufficiently far away from each other the cholesteric twist will result in a helical structure, so that the disclination lines wrap the particle surface,

https://doi.org/10.4208/nmtma.2017.s01

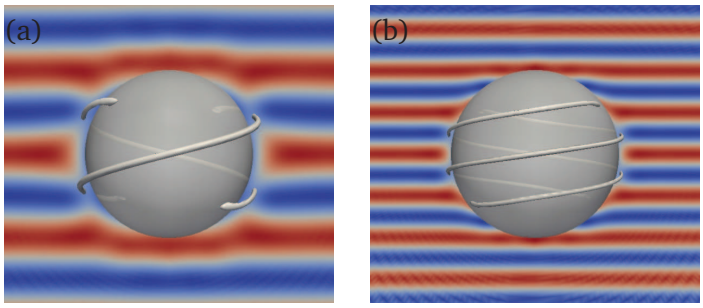

Figure 7: Helical disclination lines around planar-anchoring colloidal particles in cholesteric host. (a) $R/p = 1/2$, (b) $R/p = 1$. The background color represents the value of Q_{xx}. Defect lines are visualized by iso-surfaces of c_l.

sometimes in multiple cycles. In Fig. 7, it can be seen from the background color representing the value of Q_{xx} that the layer structure of cholesterics is only slightly disturbed, and the disturbance vanishes even more quickly than in the case of twisted Saturn rings with homeotropic anchoring. By increasing the ratio R/p, the disclination lines finish more cycles before ending on the particle surface.

When R/p is small or equal to 0, [17] describe the resulting defects as "patches" on the particle surface. In the nematic case ($R/p = 0$), the single-, double- and split- core boojums are already meticulously studied [32]. By using spectral method, we are able to plot the orientation profile with high resolution, and in this way study the detailed structure of the "patches" for small R/p, which is similar to the nematic case.

Fig. 8 shows the boojums under different ratios R/p. The other dimensionless parameters are fixed, with the dimensionless temperature $\tau = -0.3$, and $R/\xi = 40.53$. Starting from the single-core configuration in the nematic case with $R/p = 0$, we gradually increase R/p, and observed a splitting of the boojum cores similar to that in the nematic case by decreasing the dimensionless temperature or increasing the ratio R/ξ, as shown in [32]. The single-core splits into double-core with a slight increase of R/p, even as small as $1/1024$. By further increasing R/p, the pair of $+1/2$ defects composing the double-core move away from each other, turning the double-core into a split-core. The biaxial regions around the $+1/2$ defects are no longer linked on the colloidal particle surface.

This process can also be observed through the shape-change of iso-surfaces of the uniaxial order-parameter. Originally, for the nematic single-core, the iso-surfaces are rotational-symmetric convex surfaces. When cholesteric twist turns the single-cores into a split-cores, the rotational symmetry is broken, and the iso-surfaces become tubes enclosing the disclination lines, with two ends touching the particle surface. The iso-surfaces in the double-core case comes halfway in-between.

In the nematic case, for the split driven by decreasing temperature or increasing particle size, the single-core can usually be preserved for small changes of parameters, unless the values of the parameters are very close to the critical point at the start. But

https://doi.org/10.4208/nmtma.2017.s01

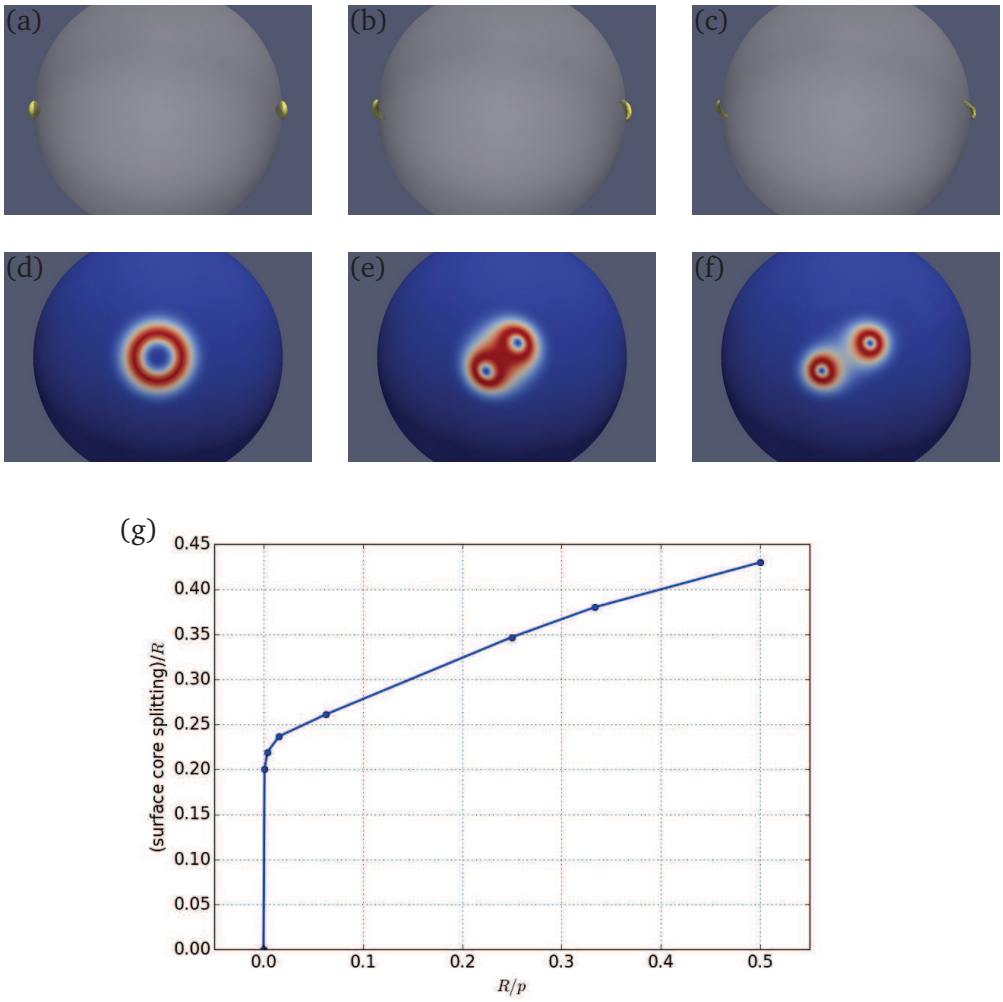

Figure 8: Boojums under different cholesteric twists. In the upper panels the iso-surfaces of nematic scalar order parameter S is shown. In the lower panels the colloidal particle surface is colored according to the biaxiality parameter β defined in expression (2.8). Red regions have high biaxiality. Types of boojum cores are: (a) and (d) single-core (nematic), (b) and (e) double-core (cholesteric $R/p = 1/64$), (c) and (f) split-core (cholesteric $R/p = 1/4$). (g) Core splitting driven by cholesteric twist. The surface core splitting is the orthodromic distance between two $+1/2$ point defects, with radius R as unit length. The defect is originally a nematic single-core.

for the split driven by cholesteric twist, the single-cores evolves into double-cores with very small change of R/p. This abrupt change can be seen in Fig. 8(g), which plots the orthodromic distance of the two $+1/2$ point defects on the particle surface. The distance rises suddenly from 0 to about $0.2R$ when R/p increases from 0 to $1/1024$. The distance further increases as R/p grows, but the increase rate slows down. The split process starting with nematic double-core or split-core boojums follows much the same pattern as the case starting with nematic single-core boojums as is described

https://doi.org/10.4208/nmtma.2017.s01

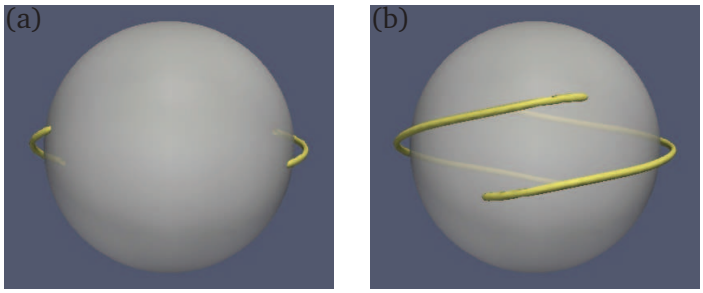

Figure 9: Disclination lines around the colloidal particle with (a) $R/p = 0.711$ (b) $R/p = 0.727$. The other dimensionless parameters are identical with those in Fig. 8. Defect lines are visualized by iso-surfaces of c_l.

above.

The defect patches, or in fact boojums as found in our simulation, evolve into helical disclination lines with further increase of R/p. This is described to happen when R/p is larger than $1/2$ in [17]. However, we find that this critical point depends on the values of τ and R/ξ. Using the values of parameters as described above, we find the critical point to be between 0.711 and 0.727. This can be seen from Fig. 9. Figs. 9(a) and (b) shows the disclination lines for $R/p = 0.711$ and 0.727 respectively. The former can be seen as patches on antipodes of the particle surface, while the latter are disclination lines wrapping around the particle. Here we can also see that the length of the disclination lines grows suddenly with small change of R/p.

5. Conclusions

In this paper, by using spectral method, we investigate the defect structures around a spherical particle in a cholesteric liquid crystal for different types of anchoring on the surface of the particle.

For strong homeotropic anchoring, we discuss two types of configurations, one is the twisted Saturn ring and the other is the cholesteric dipole, which corresponds to the nematic dipole. The cholesteric dipole we obtained is essentially different from the structures reported in [27] which is found between the cells with perpendicular anchoring on cell walls. By plotting its director field, we show that the cholesteric dipole can be regarded as a nematic dipole coupled with the cholesteric layer structure. By comparison of the free energy between the cholesteric dipole and the twisted Saturn ring, we find that the former is energetically preferable when the particle size is large compared to the nematic coherence length ξ and small compared to the cholesteric pitch p.

For strong planar anchoring, we find that the cholesteric twist results in split of the nematic boojums, and the double- and split-cores can both be obtained by applying cholesteric twist. Larger twist (larger R/p) elongates the boojums into helical disclination lines wrapping around the particle.

https://doi.org/10.4208/nmtma.2017.s01

The numerical results obtained in our simulation show the effectiveness of spectral method in dealing with this problem, as in most cases the defect configuration and orientation profile can both be captured, and fine structures of the defects made visible, by expanding $\mathrm{Q} - \mathrm{Q}_0$ into only relatively low-order terms, and the method is far more cost-efficient in terms of number of the nodes needed.

However, there are problems that our method fails to address. In order to get free energy in high accuracy, large number of terms in the expansion of $\mathrm{Q}-\mathrm{Q}_0$ is still needed, especially for large R/p and R/ξ, and the computational cost is still too great in these cases. So more work should be done to understand whether the cholesteric dipole can be stabilized with very large R/p, or if there exists a upper bound for R/p so that the cholesteric dipole cannot stably exist beyond it. Besides, we have only investigated the equilibrium state with one colloidal particle immersed in a cholesteric liquid crystal, therefore more work can be done on the situations with multiple particles and for the dynamics.

Acknowledgments P. Zhang is partly supported by National Natural Science Foundation of China (Grant No. 11421101 and No. 11421110001).

References

[1] J. M. Ball and A. Zarnescu, *Orientability and energy minimization in liquid crystal models*, Arch. Ration. Mech. Anal., 202 (2011), pp. 493–535.
[2] S. Bedford, *Global minimisers of cholesteric liquid crystal systems*, arXiv preprint arXiv: 1411.3599, (2014).
[3] A. Callan-Jones, R. A. Pelcovits, V. Slavin, S. Zhang, D. Laidlaw and G. Loriot, *Simulation and visualization of topological defects in nematic liquid crystals*, Phys. Rev. E, 74 (2006), pp. 061701.
[4] P. G. de Gennes and J. Prost, The Physics of Liquid Crystals, Oxford University Press, 1993.
[5] J. L. Ericksen, *Liquid crystals with variable degree of orientation*, Arch. Ration. Mech. Anal., 113 (1991), pp. 97–120.
[6] G. Foffano, J. Lintuvuori, A. Tiribocchi, and D. Marenduzzo, *The dynamics of colloidal intrusions in liquid crystals: a simulation perspective*, Liq. Cryst. Rev., 2 (2014), pp. 1–27.
[7] J.-B. Fournier and P. Galatola, *Modeling planar degenerate wetting and anchoring in nematic liquid crystals*, Europhys. Lett., 72 (2005), pp. 403.
[8] J. Fukuda and S. Žumer, *Cholesteric blue phases: effect of strong confinement*, Liq. Cryst., 37 (2010), pp. 875–882.
[9] J.-i. Fukuda, *Liquid crystal colloids: a novel composite material based on liquid crystals*, J. Phys. Soc. Japan, 78 (2009), pp. 041003.
[10] J.-i. Fukuda, M. Yoneya and H. Yokoyama, *Nematic liquid crystal around a spherical particle: Investigation of the defect structure and its stability using adaptive mesh refinement*, Euro. Phys. J. E, 13 (2004), pp. 87–98.
[11] H. Grebel, R. Hornreich and S. Shtrikman, *Landau theory of cholesteric blue phases*, Phys. Rev. A, 28 (1983), pp. 1114.

https://doi.org/10.4208/nmtma.2017.s01

[12] J. Han, Y. Luo, W. Wang, P. Zhang and Z. Zhang, *From microscopic theory to macroscopic theory: a systematic study on modeling for liquid crystals*, Arch. Ration. Mech. Anal., 215 (2015), pp. 741–809.
[13] R. Hornreich and S. Shtrikman, *Landau theory of twist-induced biaxiality in cholesteric liquid crystals*, Phys. Rev. A, 29 (1984), pp. 3444.
[14] Y. Hu, Y. Qu and P. Zhang, *On the disclination lines of nematic liquid crystals*, Commun. Comput. Phys., 19 (2016), pp. 354–379.
[15] T. Kato, Perturbation Theory for Linear Operators, Vol. 132, Springer Science & Business Media, 2013.
[16] J. Lintuvuori, D. Marenduzzo, K. Stratford and M. Cates, *Colloids in liquid crystals: a lattice boltzmann study*, J. Mater. Chem., 20 (2010), pp. 10547–10552.
[17] J. Lintuvuori, K. Stratford, M. Cates and D. Marenduzzo, *Colloids in cholesterics: size-dependent defects and non-stokesian microrheology*, Phys. Rev. Lett., 105 (2010), pp. 178302.
[18] L. Longa, D. Monselesan and H.-R. Trebin, *Phase diagrams of cholesteric liquid crystals obtained with a generalized landau-de gennes theory*, Liq. Cryst., 5 (1989), pp. 889–898.
[19] T. Lubensky, D. Pettey, N. Currier and H. Stark, *Topological defects and interactions in nematic emulsions*, Phys. Rev. E, 57 (1998), pp. 610.
[20] A. Majumdar, *Equilibrium order parameters of nematic liquid crystals in the landau-de gennes theory*, Euro. J. Appl. Math., 21 (2010), pp. 181–203.
[21] A. Majumdar and A. Zarnescu, *Landau–de gennes theory of nematic liquid crystals: the oseen–frank limit and beyond*, Arch. Ration. Mech. Anal., 196 (2010), pp. 227–280.
[22] M. Melle, S. Schlotthauer, C. K. Hall, E. Diaz-Herrera, and M. Schoen, *Disclination lines at homogeneous and heterogeneous colloids immersed in a chiral liquid crystal*, Soft Matter, 10 (2014), pp. 5489–5502.
[23] S. Mkaddem and E. C. Gartland, *Fine structure of defects in radial nematic droplets*, Phys. Rev. E, 62 (2000), pp. 6694–6705.
[24] I. Muševič, M. Škarabot, U. Tkalec, M. Ravnik and S. Žumer, *Two-dimensional nematic colloidal crystals self-assembled by topological defects*, Science, 313 (2006), pp. 954–958.
[25] L. Onsager, *The effects of shape on the interaction of colloidal particles*, Ann. N. Y. Acad. Sci., 51 (1949), pp. 627–659.
[26] C. Oseen, *The theory of liquid crystals*, Trans. Faraday Soc., 29 (1933), pp. 883–899.
[27] M. Pandey, P. Ackerman, A. Burkart, T. Porenta, S. Žumer and I. I. Smalyukh, *Topology and self-assembly of defect-colloidal superstructure in confined chiral nematic liquid crystals*, Phys. Rev. E, 91 (2015), pp. 012501.
[28] P. Poulin, H. Stark, T. Lubensky, and D. Weitz, *Novel colloidal interactions in anisotropic fluids*, Science, 275 (1997), pp. 1770–1773.
[29] P. Poulin and D. Weitz, *Inverted and multiple nematic emulsions*, Phys. Rev. E, 57 (1998), pp. 626.
[30] M. Ravnik and S. Žumer, *Landau–de gennes modelling of nematic liquid crystal colloids*, Liq. Cryst., 36 (2009), pp. 1201–1214.
[31] J. Shen, T. Tang, and L.-L. Wang, *Spectral Methods: Algorithms, Analysis and Applications*, Vol. 41, Springer Science & Business Media, 2011.
[32] M. Tasinkevych, N. Silvestre and M. T. da Gama, *Liquid crystal boojum-colloids*, New J. Phys., 14 (2012), pp. 073030.

https://doi.org/10.4208/nmtma.2017.s01